AGU PUBLICATIONS

JGR

Journal of Geophysical Research: Oceans

RESEARCH ARTICLE

10.1002/2013JC009513

Key Points:
- Enlargement of Pine Island ice shelf cavity has let to rapid increase of melt
- A subglacial sill controls the sensitivity of melt to ocean variability
- At present, melt rates are modulated by changes in ocean heat content

Correspondence to:
J. De Rydt,
janryd69@bas.ac.uk

Citation:
De Rydt, J., P. R. Holland, P. Dutrieux, and A. Jenkins (2014), Geometric and oceanographic controls on melting beneath Pine Island Glacier, *J. Geophys. Res. Oceans*, *119*, 2420–2438, doi:10.1002/2013JC009513.

Received 18 OCT 2013
Accepted 20 MAR 2014
Accepted article online 24 MAR 2014
Published online 15 APR 2014

Geometric and oceanographic controls on melting beneath Pine Island Glacier

J. De Rydt[1], P. R. Holland[1], P. Dutrieux[1], and A. Jenkins[1]

[1]British Antarctic Survey, Natural Environment Research Council, Cambridge, UK

Abstract Observations beneath the floating section of Pine Island Glacier have revealed the presence of a subglacial ridge which rises up to 300 m above the surrounding bathymetry. This topographic feature probably served as a steady grounding line position until sometime before the 1970s, when an ongoing phase of rapid grounding line retreat was initiated. As a result, a large ocean cavity has formed behind the ridge, strongly controlling the ocean circulation beneath the ice shelf and modulating the ocean water properties that cause ice melting in the vicinity of the grounding line. In order to understand how melt rates have changed during the various phases of cavity formation, we use a high-resolution ocean model to simulate the cavity circulation for a series of synthetic geometries. We show that the height of the ridge and the gap between the ridge and ice shelf strongly control the inflow of warm bottom waters into the cavity, and hence the melt rates. Model results suggest a rapid geometrically controlled increase of meltwater production at the onset of ice thinning, but a weak sensitivity to geometry once the gap between the ridge and ice shelf has passed a threshold value of about 200 m. This provides evidence for a new, coupled, ice-ocean feedback acting to enhance the initial retreat of an ice stream from a bedrock high. The present gap is over 200 m, and our results suggest that observed variability in melt rates is now controlled by other factors, such as the depth of the thermocline.

1. Introduction

The dynamics of many Antarctic ice streams are controlled by the presence of floating ice shelves, which form at the grounding line and extend into the adjacent sea, where they lose ice through basal melting and iceberg calving. Recent observations have shown that many ice shelves in West Antarctica and around the Antarctic Peninsula are undergoing dramatic changes, with a consistent decrease in extent and thickness, and a complete disintegration of some shelves [*Cook and Vaughan*, 2010; *Pritchard et al*., 2012]. This has resulted in accelerated glacier flow, grounding line retreat and increased discharge of grounded ice into the ocean [*Shepherd et al*., 2012; *Park et al*., 2013].

The region undergoing some of the most dramatic changes is the coastline of the Amundsen Sea (Figure 1, inset), where the 200–1000 m thick ice shelves have thinned by up to 5.9 m a^{-1} over the period from 1992 to 2001 [*Shepherd et al*., 2004], and up to 6.8 m a^{-1} from 2003 to 2008 [*Pritchard et al*., 2012]. Most of this thinning can be attributed to increased basal melting, caused by the interaction of the deepest ice with lightly modified Circumpolar Deep Water (CDW) [*Jacobs et al*., 2011]. This relatively warm ($\sim$1°C) and saline ($>$34.5) water originates in the Antarctic Circumpolar Current offshore of the continental shelf break [*Jacobs et al*., 1996]. A combination of dynamical processes at the shelf edge, such as the interaction between the shelf-edge currents and the topography of the shelf break, drive the CDW into cross-shelf troughs which lead toward the grounding zone of the ice sheet [*Walker et al*., 2007; *Thoma et al*., 2008; *Wahlin et al*., 2010; *Walker et al*., 2013; *Assmann et al*., 2013]. Although the mechanisms that modulate the on-shelf transport of warm water are not fully understood, it is suspected that a net increase of heat onto the continental shelf has been an important driver for the thinning of the adjacent ice shelves [*Shepherd et al*., 2004]. Numerical simulations of ocean processes in the Amundsen Sea indeed relate temporal variability in ice-shelf melt rates to variability in the shelf edge heat fluxes [*Thoma et al*., 2008]. On the other hand, a model-based study by *Schodlok et al*. [2012] stresses the importance of local ocean-atmosphere forcing over the inner shelf.

Observations at the calving front of Pine Island Glacier (PIG), one of the largest outlet glaciers in the Amundsen sector, have confirmed the presence of CDW below a depth of 600 m [*Jacobs et al*., 1996; *Jenkins et al*., 2010a; *Jacobs et al*., 2011; *Dutrieux et al*., 2014]. In addition, measurements beneath the ice shelf have shown

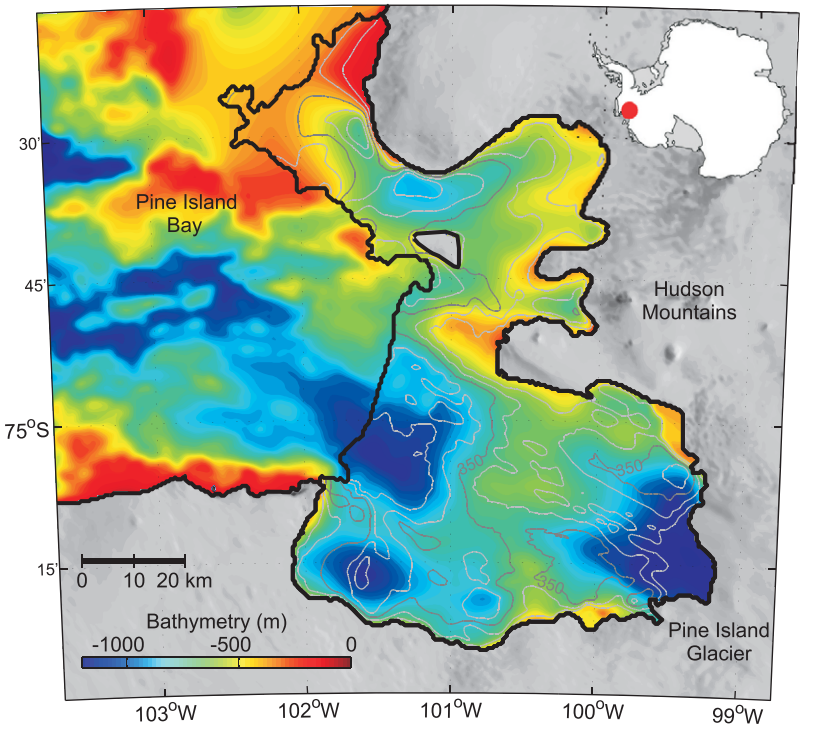

Figure 1. Bathymetry in Pine Island Bay and under the Pine Island Glacier ice shelf, West-Antarctica (see inset). The ice shelf is outlined by the black contour, corresponding to its 2009 grounding line [*Joughin et al.*, 2010] and calving front position. Grounded ice is portrayed by a subset of the MODIS mosaic for Antarctica [*Scambos et al.*, 2006]. A seabed trough extends from the northwest to the deep grounding line in the southeast, interrupted by a 300 m high ridge that extends north-south at roughly 101.5°W. The water column thickness above the ridge is bounded by the 350 m contour, represented in dark gray. Other contour levels at 100 m intervals are shown in light gray.

that modified CDW is able to penetrate to the 1000 m deep grounding line of the glacier [*Jenkins et al.*, 2010a], where it contains enough heat to produce melt rates in excess of 100 m a^{-1} [*Dutrieux et al.*, 2013]. Between 1994 and 2008, satellite data have shown that on average the PIG ice shelf has lost a volume of 36 ± 4 km^3 a^{-1} [*Shepherd et al.*, 2010], despite a twofold increase in glacier discharge across the grounding line. As there are no indications of a significant trend in surface accumulation in the region [*Medley et al.*, 2013], and firn models suggest a modest thickening of the firn layer during this period [*Ligtenberg et al.*, 2011; *Pritchard et al.*, 2012], it is clear that the main contributor to the mass imbalance of the ice shelf is submarine melt, caused by the interaction with the surrounding warm ocean water [*Rignot et al.*, 2013].

The accelerated thinning of the ice shelf has led to a near-continuous retreat of the grounding line between 1992 and 2011 [*Rignot*, 1998; *Joughin et al.*, 2010; *Park et al.*, 2013], with its present day location situated approximately 20 km inland of the 1992 position. The onset of retreat predates 1992, as changes in surface expressions obtained from Landsat imagery indicate the loss of a pinning point downstream of the 1992 grounding line during the late 1970s [*Jenkins et al.*, 2010a]. Under-ice measurements of the bathymetry [*Jenkins et al.*, 2010a], as well as gravimetry data [*Muto et al.*, 2013], have shown that the location of this pinning point coincides with a prominent subglacial ridge, which stretches north-south, transverse to the prevailing ice flow direction, and rises about 300 m above the surrounding bathymetry (Figure 1). This seabed feature probably served as a temporary steady grounding line position for PIG prior to its present day retreat.

The unpinning and rapid retreat of PIG from the bathymetric ridge has led to the formation of a large ocean cavity behind the ridge, exposing a larger and deeper part of the ice sheet to warm ocean waters. Although the ridge provides a topographic barrier that impedes the inflow of the deepest shelf waters, lightly modified CDW was found in the inner cavity in 2009, exposing the present day ice base to ocean temperatures about 4° above the in situ freezing point [*Jenkins et al.*, 2010a]. Observations and numerical simulations of the buoyancy-driven cavity circulation [*Heimbach and Losch*, 2012; *Dutrieux et al.*, 2014] also suggest the presence of a strong, topographically steered cyclonic flow inshore of the ridge, which intensifies the vertical turbulent mixing of heat toward the ice-ocean interface. The amount of heat exchange across the ridge and the level of

turbulent mixing modulate the basal melt rate, and changes to both processes during the enlargement of the PIG cavity are likely to have led to important temporal variability in meltwater production.

It is well known that variations in ice shelf draft have a strong effect on melting [*Holland et al*., 2008b; *Little et al*., 2009; *Gladish et al*., 2012; *Dutrieux et al*., 2013]. However, the processes that relate changes in melt rate to geometrical changes of the ice shelf cavity in the presence of a ridge have remained unexplored to date, although they are essential for our understanding of the past and future evolution of ice-ocean dynamics underneath PIG. One of the challenges that needs to be overcome is the lack of reliable data about the shape of the under-ice cavity. A coarse-resolution ice draft data set was derived for the 1994 PIG ice draft by *Payne et al*. [2007], and used in combination with a two-dimensional plume model to simulate the spatial distribution of melting. A higher resolution product for the 2009 ice draft and seabed depth was created by *Dutrieux et al*. [2014], and used in a full three-dimensional ocean model. No ice shelf-wide data are available for other time periods, hence impeding a systematic study of changes in ice melt due to changes in the cavity geometry. In addition, large uncertainties still remain in most of the seabed bathymetry, despite the Autosub3 mission [*Jenkins et al*., 2010a].

In this study, we overcome the sparsity of data and provide an alternative for understanding the temporal evolution of melt rates by using a series of simplified, synthetic cavity shapes that capture the main geometrical features of the PIG ice shelf cavity during various stages of its enlargement. We assume that the dominant ocean processes that regulate the melt rate are reproduced by these simplified geometries, and those processes that require a detailed knowledge of the cavity geometry can be discarded in first approximation. We do not aim to simulate the small-scale distribution of melt rates, despite its suggested importance for ice-ocean interactions, in particular in the presence of ice shelf basal channels [*Payne et al*., 2007; *Rignot and Steffen*, 2008; *Gladish et al*., 2012; *Vaughan et al*., 2012; *Mankoff et al*., 2012; *Dutrieux et al*., 2014]. Broad-scale ocean dynamics for the simplified geometries can be compared to observational data obtained in 2009, and observational uncertainties in the bedrock topography are accommodated through sensitivity tests in which the height of the subglacial ridge is varied. As an additional advantage, the synthetic approach allows to fully isolate the dynamical effects of the ridge through a comparison with model results for a flat bathymetry.

In addition to changes in the geometry, variability of the melt rates can in part be attributed to changing ocean conditions. Repeated CTD measurements at the PIG ice front have revealed interannual variability in the temperature structure and melt water content of the upper 800 m [*Jacobs et al*., 2011], with a general increase of the ocean heat content up to 2009. This apparently persistent trend was interrupted in 2012 by a decrease of 53% in the meltwater volume as compared to 2009, in combination with an anomalously deep thermocline which dropped 200 m below the 2009 level [*Dutrieux et al*., 2014]. Although the onset of the current retreat and thinning of PIG remains the subject of investigation, an increased ocean heat content at the ice base related to the enhanced transport of CDW toward the PIG grounding line is thought to be the main driver. In order to assess the sensitivity of modeled melt rates to changes in the ocean heat content, and to quantify the relative importance compared with changes in the ice shelf geometry, we present the results from a sensitivity study in which the thermocline is lowered by 100 and 200 m, respectively, with respect to 2009 conditions.

The paper is structured as follows. In section 2, we introduce the model setup and describe geometric and hydrographic boundary conditions for the ocean dynamics. A concise summary is given of the ice-ocean interactions implemented in the model. In section 3, model results are presented for the default setup, which is an idealized representation of the cavity geometry and hydrographic conditions observed in 2009. A qualitative comparison to observational data is given, in order to validate and justify the simplifications made. In subsequent sections, the results for various sensitivity experiments are presented, describing the changes in ocean circulation and melt rates during cavity formation (section 4), for different hydrographic forcing conditions at the ice front (section 5), and for a variable height of the seabed ridge (section 6). Results are discussed in section 7, and conclusions drawn in section 8.

2. Modeling Approach

2.1. Model Setup

Ocean processes in the subice shelf cavity are simulated using the three-dimensional MITgcm [*Marshall et al*., 1997], modified by *Losch* [2008] to include the pressure loading and thermodynamic forcing of a

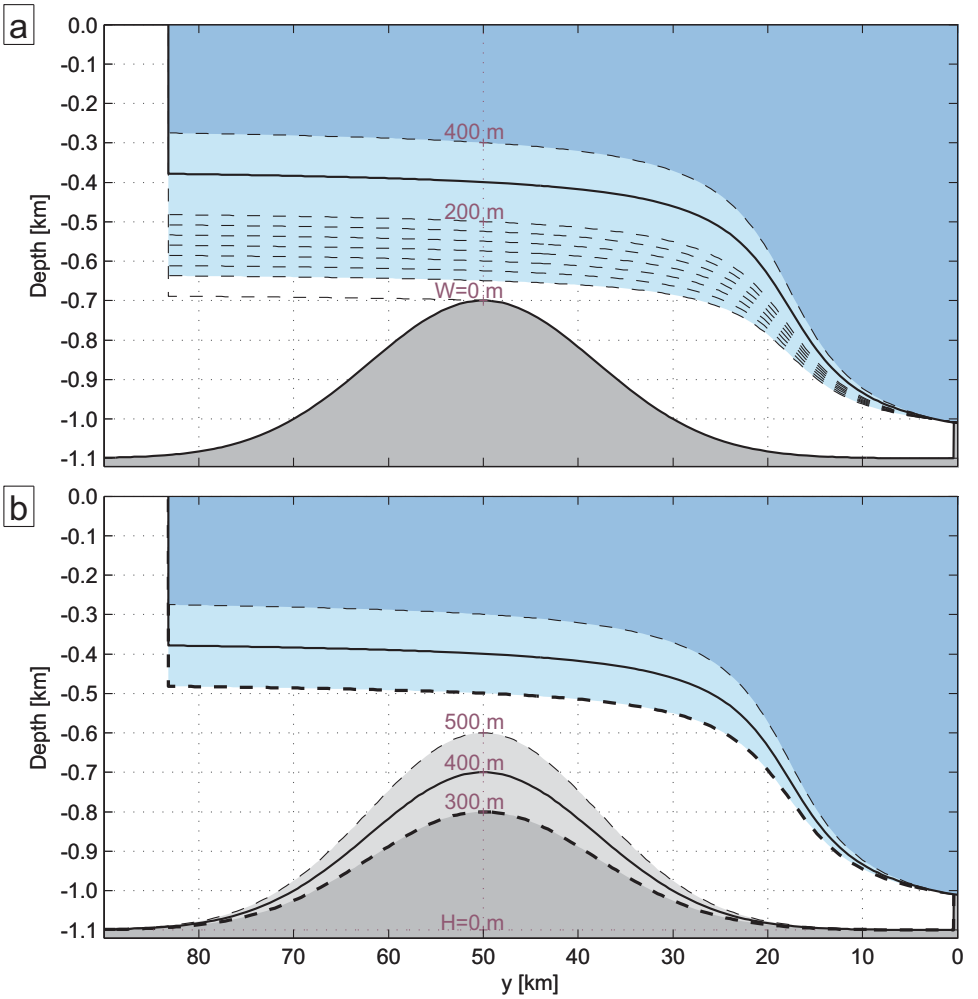

Figure 2. (a) Dashed lines delineate synthetic ice shelf geometries that are used to simulate the effects of ice shelf cavity formation on ocean circulation and melt rates. Different geometries have different values of water column thickness (parameterized by *W*) at the ridge top. The dimensions of the domain and geometry are representative for the fast flowing region of Pine Island Glacier ice shelf. The solid black line is an idealized representation of the ice geometry observed in 2009 [*Jenkins et al*., 2010]. (b) Dashed lines represent the cavity geometry for different heights of the subglacial ridge (parameterized by *H*), while the water column thickness at the ridge crest is kept constant at $W = 300$ m. The solid line is an idealized representation of the 2009 geometry.

steady ice shelf. The MITgcm is a *z*-coordinate model with partial-cell treatment of the topography, allowing an accurate description of the cavity geometry. Our model grid consists of 110 layers with a vertical spacing of 10 m, and a horizontal resolution of 400 m. Advection is modeled by a third-order flux-limited advection scheme, and constant values of 15 and 2.5 $m^2\ s^{-1}$ are used for horizontal Laplacian viscosity and horizontal diffusivity. Vertical mixing is parameterized by the Pacanowski-Philander scheme with original parameter values [*Pacanowski and Philander*, 1981]. Each simulation is run for 18 months, after which a quasi steady state is reached, and all results presented are an average over the final month. The model is used in its hydrostatic configuration because experimentation with the nonhydrostatic solver showed little appreciable difference in the results.

2.2. Ice Shelf Geometry and Bathymetry

The model is primarily used to investigate differences in ocean circulation and melt rates for different geometries of the subice shelf cavity. As our knowledge of PIG ice shelf thickness variations is limited in both space and time, and the bathymetry remains poorly constrained, a series of synthetic geometries is created that capture the main features of the cavity. The longitudinal (*x*), latitudinal (*y*), and vertical dimensions of the model domain are 48 km, 128 km, and 1100 m, respectively. The ice draft and bathymetry are uniform in the zonal direction; meridional profiles are depicted in Figures 2a and 2b. Note that in reality PIG is

oriented approximately east-west (Figure 1), but we discuss our idealized ice shelf as if the ice flowed north, following the convention in previous idealized modeling studies [e.g., *Grosfeld et al*., 1997]. The different orientation of the model domain does not affect the results, as the beta-effect is negligible for our domain size.

For simplicity, the cavity geometry is uniquely determined by two parameters, denoted by H and W. The first parameter, H, specifies the height of the bathymetric ridge above the surrounding seabed. The ridge is represented by a Gaussian profile with a maximum elevation at 50 km from the grounding line, and a full width at half maximum of ∼28 km. The position and size of the ridge are inspired by the realistic geometry in Figure 1. The second parameter, W, specifies the water column thickness at the ridge top, and uniquely determines the ice draft for any given value of H. The position of the grounding line is kept fixed at 1000 m depth, except when $W = 0$ m for which the ice shelf is grounded on top of the ridge. In the following, specific cavity geometries will be referred to as a pair (H_{z_1}, W_{z_2}), where the subscripts specify the values of H and W. For example, (H_{400}, W_{300}) refers to the geometry with bathymetry $b(y, H = 400\,m)$ and ice draft $h(y, H{=}400\,m, W{=}300\,m)$. This particular cavity shape is highlighted by the solid lines in Figure 2, and corresponds to an idealized representation of the ice shelf draft and bathymetry as measured in 2009 by the Autosub3 submersible [*Jenkins et al*., 2010a].

In this study, we consider two sets of geometrical experiments in which H and W are varied independently. In a first set of sensitivity tests, we simulate melt rates for the PIG ice shelf during various stages of its thinning and retreat from the subglacial ridge. For that purpose, H is kept fixed at 400 m and W takes values of 0 m, from 50 to 200 m with 25 m intervals, and from 200 to 400 m with 100 m intervals. This set of geometries is used to simulate the gradual opening of a gap between the ice base and the subglacial ridge, and the formation of a cavity upstream of the ridge. The different shapes of the ice draft are represented by dashed lines in Figure 2a. The minimum nonzero value for W is restricted by the vertical resolution of the model, as we impose a minimum water column thickness of 50 m, corresponding to five vertical grid cells.

In a second set of geometrical experiments, we test the sensitivity of our results to uncertainties in the bedrock geometry. The value of W is kept fixed at 300 m while the amplitude of the ridge is varied from $H = 300$ m to $H = 500$ m. This is within the range of uncertainty for the gravity observations [*Muto et al*., 2013]. The different shapes of the bathymetry and corresponding ice drafts are presented in Figure 2b. In addition, we compare these results to model simulations with a flat bathymetry, in order to isolate the impact of the subglacial ridge on the ocean dynamics and melt rates.

It should be noted that the ice profiles in this study are not obtained from ice-dynamics considerations, and instead a simple inverse tangent curve is used:

$$h(y,H,W)=\begin{cases}\left(\dfrac{-90+W+H}{2.64}\right)\tan^{-1}\left(\dfrac{y}{5882}-3\right) & \\ \qquad +0.47(W+H)-1051.3 & \text{for } y < 84\,\text{km} \\ 0 & \text{for } y \geq 84\,\text{km}\,,\end{cases} \tag{1}$$

where $y = 84$ km determines the position of the ice front. This choice is partly motivated by the fact that more realistic shapes of the ice shelf are strongly related to basal melt rates, which are a priori unknown, and by the fact that simple analytical solutions of the ice dynamics equations [see e.g., *Van der Veen*, 1985] do not satisfy the geometrical properties observed for the PIG ice shelf. In order to find a state where ice and ocean dynamics are in mutual balance, coupled ice-ocean simulations are required, which are beyond the scope of this work. Instead, we investigate the interaction of the ocean with a static ice shelf, and show that leading-order changes in ocean circulation are related to the values of the parameters W and H.

2.3. Hydrographic Forcing

Solid walls with a free-slip condition constrain the ocean flow at the southern, western and eastern sides of the domain. At the northern boundary, in addition to a no-normal flow condition, restoring conditions for the temperature and salinity are prescribed. The restoring timescale varies linearly across a 2 km wide margin, from 12 h at the boundary to 60 h in the interior. The temperature and salinity profiles imposed at the

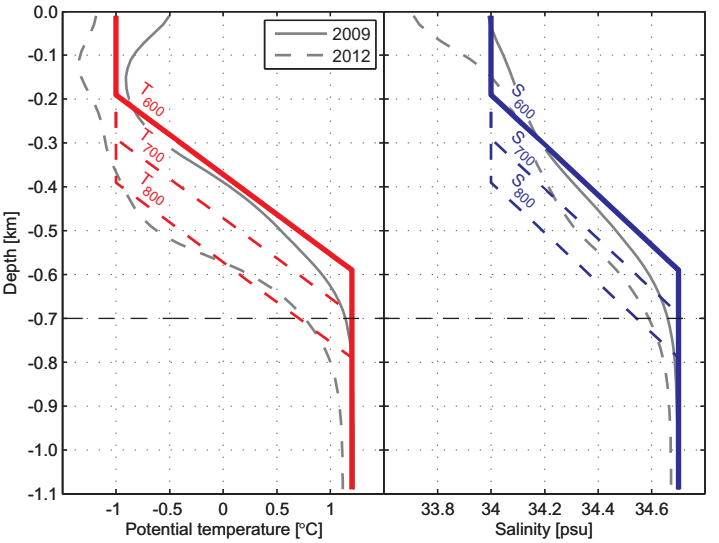

Figure 3. Solid red and blue lines, labeled by T_{600} and S_{600}, respectively, depict temperature and salinity restoring conditions applied at the northern boundary of the model domain. Subscripts for T and S indicate the depth of the thermocline and halocline. Dashed lines are profiles used in section 5. to study the sensitivity of melt rates to the pycnocline depth. Gray lines correspond to average temperature and salinity conditions taken from CTD measurements in Pine Island Bay during the austral summers of 2009 [*Jacobs et al.*, 2011] and 2012 [*Dutrieux et al.*, 2014]. They closely follow the synthetic temperature profiles with the bottom of the thermocline extending down to 600 m (2009) and 800 m (2012). The dashed line at −700 m indicates the elevation of the ridge crest in the default setup.

northern boundary are depicted by the solid red and blue curves in Figure 3, and are labeled by T_{600} and S_{600}. The subscripts for T and S denote the bottom depth of the thermocline and halocline, respectively.

The imposed temperature and salinity sections correspond to hydrographic conditions that are characteristic for the Pine Island Bay [*Jacobs et al.*, 1996], with a cold (−1°C) and fresh (34) layer of Winter Water close to the surface freezing temperature overlaying a layer of warm (1.2°C) and saline (34.7) Circumpolar Deep Water (CDW) with temperatures up to 4°C above the in situ freezing point. The two water masses are assumed to have constant properties with depth, and are joined by a pycnocline with linearly varying temperature and salinity. For comparison, Figure 3 shows averaged temperature and salinity sections obtained from 89 CTD casts taken in the austral summer of 2009 in Pine Island Bay [*Jacobs et al.*, 2011]. The piecewise linear temperature and salinity profiles used in this study closely follow the 2009 observations, with a thermocline and halocline which extend down to a depth of about 600 m.

A record of hydrographic conditions in Pine Island Bay during the austral summers of 1994, 2000, 2007, 2009, 2010, and 2012 shows, however, that the depth of the thermocline, and to a lesser extent the halocline, varies considerably on interannual timescales [*Jacobs et al.*, 2011; *Dutrieux et al.*, 2014]. The hydrographic conditions measured in 2012, which are the coldest on record, are also shown in Figure 3, and reveal a ≈200 m deepening of the thermocline compared to 2009. A reconstruction of meltwater budgets from measurements at the PIG ice front indicates that, as a result, melt rates are halved between years with a shallow (e.g., 2009) and deep (e.g., 2012) thermocline [*Dutrieux et al.*, 2014]. In order to assess the dependence of modeled melt rates on thermocline depth, we perform a series of sensitivity experiments in which the temperature forcing at the boundary is varied by moving the thermocline and halocline down by 100 and 200 m. This is shown by the curves (T_{700}, S_{700}) and (T_{800}, T_{800}) in Figure 3. The profile with the deepest thermocline follows the 2012 observations.

2.4. Modeling Ice-Ocean Processes

The basal melt rate m (positive for melting) is determined by the exchange of heat and salt across the ice-ocean boundary, and can be modeled by a system of three equations which express the conservation of heat and salt, in addition to a linear relation between freezing temperature and salinity [*Holland and Jenkins*, 1999]:

$$\rho_O c_{pO} \gamma_T (T - T_b) = m \rho_O L + \rho_I c_{pI} \kappa_I \left(\frac{T_b - T_I}{H_I} \right), \tag{2}$$

$$\gamma_S (S - S_b) = m S_b, \tag{3}$$

$$T_b = a S_b + b + c p_b, \tag{4}$$

where $\rho_O = 1030$ kg m^{-3} and $\rho_I = 917$ kg m^{-3} are the ocean and ice reference densities; $c_{pO} = 3947$ J kg^{-1} °C^{-1} and $c_{pI} = 2000$ J kg^{-1} °C^{-1} are the specific heat capacities of water and ice; T and S are the temperature and salinity of the ambient ocean; T_b, S_b, and p_b are the temperature, salinity, and pressure at the ice-ocean interface; $L = 3.34 \times 10^5$ J kg^{-1} is the latent heat of fusion; $\kappa_I = 1.54 \times 10^{-6}$ m^2 s^{-1} is heat diffusivity through the ice shelf; $T_I = -20$°C is the internal ice shelf temperature; H_I is the ice shelf thickness; and $a = -0.0575$°C, $b = 0.0901$°C, and $c = -7.61 \times 10^{-8}$°CPa^{-1}.

Following *Holland and Jenkins* [1999], the heat and salt exchange coefficients γ_T and γ_S are, to leading order, linear in the friction velocity u_* at the ice-ocean interface:

$$\gamma_{T,S} = \frac{u_*}{\Gamma_{\text{Turb}}(u_*) + \Gamma^{T,S}_{\text{Mole}}}, \tag{5}$$

where u_* is defined via a quadratic drag law, $u_* = \sqrt{c_d u_O^2}$, with $c_d = 2.5 \times 10^{-3}$ a dimensionless drag parameter and u_O the ocean velocity next to the ice shelf base. The implementation of this parameterization in MITgcm is studied in more detail in [*Dansereau et al.*, 2014]. (doi:10.1002/2013JC008846)

An expression for the velocity-dependent turbulent transfer parameter $\Gamma_{\text{Turb}}(u_*)$, and the constant thermal and haline molecular transfer parameters $\Gamma^{T,S}_{\text{Mole}}$ can be found in *Holland and Jenkins* [1999]. Typical values for u_* are on the order of 5×10^{-3} m s^{-1}, which results in values for $\gamma_T u_*$ and $\gamma_S u_*$ on the order of 0.011 and 4.4×10^{-4}, respectively. These numbers agree well with the recommended values $\Gamma_T = 0.0112$ and $\Gamma_S = 3.14 \times 10^{-4}$, obtained by *Jenkins et al.* [2010b] from measurements at the base of the Ronne Ice Shelf.

In the MITgcm, the three equations (2–4) are solved simultaneously for the free variables m, T_b, and S_b, using vertically averaged values of T, S, and u_* over a 10 m thick boundary layer. This use of a boundary layer scheme reduces the noise caused by the partial-cell representation of the ice draft, and produces a relatively smooth field of melt rates [*Losch*, 2008]. Following the conservative formulation of *Jenkins et al.* [2001], the melt rate is converted into a freshwater flux, which is applied to the boundary layer by means of a virtual salt flux to keep the ocean volume constant.

3. Results for the Default Geometry

Previous studies address ocean dynamics and ice shelf melting for a variety of synthetic ice-shelf geometries [*Grosfeld et al.*, 1997; *Losch*, 2008; *Holland et al.*, 2008a; *Little et al.*, 2009]. In all cases, a flat or uniformly sloping seabed allows hydrographic boundary conditions to propagate uninterrupted to the ice shelf base, where they set the ambient ocean conditions that drive the melting. Our model setup differs from previous work as the nontrivial bedrock topography provides a barrier which prevents the deepest water masses outside the cavity from reaching the ice base directly. As a result, modified properties of the ambient ocean layer and changes in the topographically steered flow have an important effect on simulated ice shelf melt rates. In this section, we present the results from a simulation with default 2009 like cavity geometry (H_{400}, W_{300}) and hydrographic restoring conditions (T_{600}, S_{600}), as depicted by the solid lines in Figures 2a and 3, respectively. This simulation allows us to investigate the general flow characteristics, and provides benchmark results for further sensitivity tests.

Melt rates for the default setup are shown in Figure 4a, and vary from <10 m a^{-1} north of $y = 30$ km to values up to 120 m a^{-1} for the western boundary current and steep parts of the ice base near the grounding line. The spatially averaged melt rate is 26.6 m a^{-1} and the total meltwater volume amounts to 107 km^3 a^{-1}. Despite the high level of simplification in the ice shelf geometry, bathymetry, and hydrographic forcing, these model results are relatively close to realistic estimates of the average melt rate (33 ± 2 m a^{-1}) and the total meltwater volume (85 ± 6 km^3 a^{-1}) beneath the fast-flowing region of PIG ice shelf in 2009 [*Jacobs et al.*, 2011].

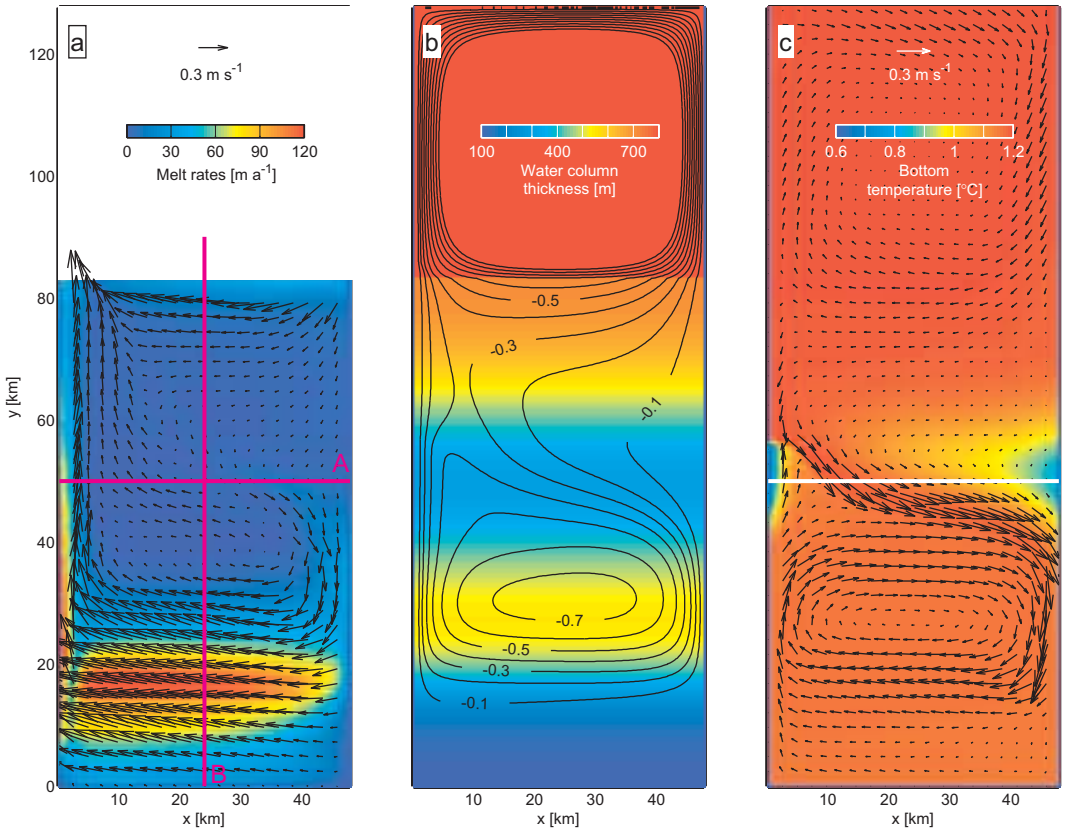

Figure 4. Summary of ice-ocean properties for the default simulation with geometry (H_{400}, W_{300}) and forcing (T_{600}, S_{600}). (a) Melt rates (colors) and ocean velocities u_O (arrows) averaged over the 10 m boundary layer and plotted every sixth horizontal grid cell. Magenta lines indicate the *xy* location of the sections A and B, shown in Figure 5. (b) Water column thickness (colors) and the barotropic stream function (contours, in units of Sv). (c) Potential temperature and corresponding circulation averaged over the bottom 20 m.

Melt rates are directly related to the ocean circulation u_O (equations (2), (3), and (5)). In Figure 4a, the velocities u_O form a Coriolis-driven cyclonic circulation that is directed southward at the eastern boundary, has a dominant westward direction south of $y = 30$ km, and a northward current at the western boundary. A westward flow near the ice front follows the cyclonic circulation in the open ocean, which does not acquire its momentum from buoyancy effects. Instead, it is driven by a sustained density gradient imposed by the restoring conditions at the northern boundary. This circulation, with speeds up to 0.5 m s^{-1}, represents a real cyclonic circulation observed in Pine Island Bay [*Jacobs et al.*, 2011]. Overall, a strong spatial correlation ($r^2 = 0.82$) between $|u_O|$ and m is apparent in Figure 4a, as high (low) melt rates coincide with a strong (weak) current in the ice-ocean boundary layer. This is a result of the parametrization of γ_T in terms of u_* (equation (5)).

Further understanding of the cavity circulation can be obtained from the (depth integrated) barotropic stream function, which is depicted in Figure 4b. In agreement with the boundary layer circulation u_O, there is a net inflow at the ice front in the east, and a stronger outflowing boundary current in the west. This pattern is characteristic for any idealized ice shelf in the southern hemisphere, as the buoyancy driving force is balanced by Coriolis effects at small Rossby number. Underneath the ice shelf, the barotropic circulation is primarily constrained by the geometry, and streamlines tend to align east-west with contours of constant water column thickness (h_W; colors in Figure 4b). The ridge acts as a potential vorticity barrier, which causes a topographically trapped circulation to spin up in the cavity inshore of the ridge. In the ocean interior, potential vorticity is dominated by the planetary vorticity f/h_W, where $f = -1.4 \times 10^{-4}$ s^{-1} is the Coriolis parameter at 75°S. Closer to the boundaries, flow divergence and relative vorticity allow flow perpendicular to contours of constant h_W, and induce a southward (northward) flow in the east (west). The general cavity circulation is surprisingly similar to more realistic simulations presented by *Heimbach and Losch* [2012] and *Dutrieux et al.* [2014], despite the lack of geometrical details.

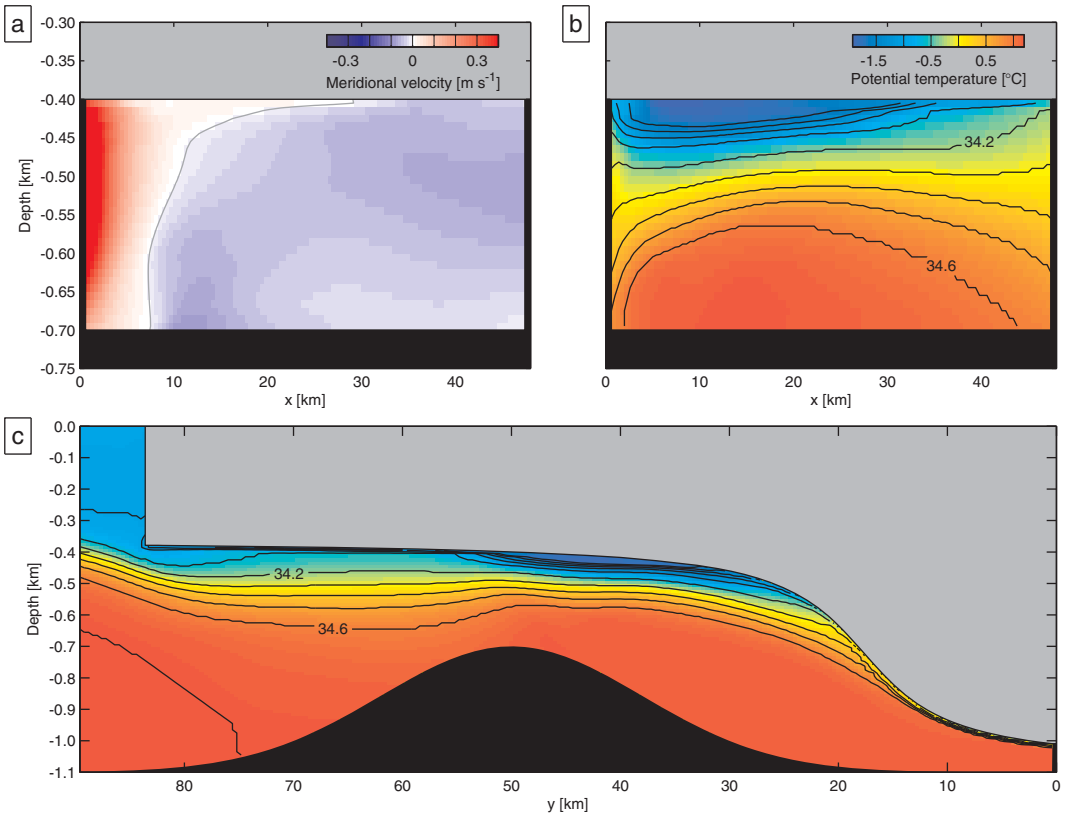

Figure 5. (a) Meridional velocities along section A, indicated by the magenta line in Figure 4a. The section stretches from (left) west to (right) east across the ridge crest, hence facing toward the ice front. The zero-velocity contour is shown in gray. (b) Potential temperature (colors) and salinity (contours) along section A. (c) Potential temperature and salinity along section B, indicated by the magenta line in Figure 4a.

In our setup, the warmest water outside the ice shelf cavity (1.2°C) is found below a depth of 600 m. Figure 4c shows that this bottom water enters the cavity in the east, and is able to flow across the bathymetric ridge (white line) at around $x = 12$ km, from where it penetrates to the grounding line in a largely unmodified form. The meridional component of the flow at the ridge crest (Figure 5a) is largely barotropic, with a southward component in the central and eastern parts of the domain, and a strong northward boundary current in the west. The corresponding temperature and salinity section in Figure 5b shows a meltwater plume with variable thickness, and a large volume of warm, saline water which rises above the ridge crest. At $x = 0$ km and $x = 48$ km, downward mixing of colder and fresher meltwater causes a net cooling of the lower layers. This has an important effect on the water mass properties that eventually flush the inner cavity and supply heat to the inner region that is most susceptible to melting. Indeed, Figure 4c implies that colder and fresher waters at the bottom of the western and eastern boundaries mix with the inflowing warm water, cooling, and freshening the latter. Although this process is negligible here, vertical and horizontal mixing and associated cooling at the ridge crest will play an important role for geometries with $W \leq 200$ m (section 4).

The persistence of warm water inshore of the ridge is illustrated in Figure 5c by a meridional section of temperature and salinity along the middle of the domain. A comparison of Figure 5c to observations underneath the PIG ice shelf [*Jenkins et al.*, 2010a] shows that our simplified geometry reproduces the main hydrographic features relatively well: warm saline water reaches the grounding line; the shallow ocean boundary layer at the ice interface deepens and is coldest inshore of the ridge; and a weak hydrographic front forms on the northern slope of the ridge, resulting in a nonzero zonal component of the flow. Compared with observations, warm waters in the model are too dominant in the inner cavity, which can be related to simplifications and possible uncertainties in the cavity geometry.

4. Sensitivity of Ocean Circulation and Melt Rates to Cavity Geometry

For a steady ice shelf and forcing, the model reaches an equilibrium between the buoyancy-driven flow and corresponding melt water production. However, for realistic systems which are out of equilibrium, such as the PIG ice shelf, continuous changes to the cavity geometry induce temporal variability in the cavity circulation and melt rates. In order to understand these changes, and to identify potential feedback mechanisms between the geometry, ocean circulation, and basal melt rates, we present results from a sensitivity test with different shapes of the ice shelf, as depicted in Figure 2. The geometries considered are simple vertical deformations of the default shape, i.e., W is varied from 0 to 400 m, in order to simulate the gradual opening of a gap between the ice base and the subglacial ridge, and the formation of a cavity upstream of the ridge. All other model parameters, including the temperature and salinity forcing at the boundary (T_{600} and S_{600}) and the bathymetry (H_{400}), are kept fixed throughout these simulations.

The total freshwater flux for each geometry, i.e., the area integral of meltwater production, is shown in Figure 6a. The corresponding mean melt rate is indicated on the right axis, and is proportional to the freshwater flux because the melting area of the ice shelf is constant for $W > 0$ (in the MITgcm melting only occurs on the horizontal faces of the step-like ice-ocean interface, i.e. faces in the x–y plane.). For $W = 0$ m, the ice shelf is grounded at the ridge crest and reaches a depth of 700 m, i.e., 100 m below the bottom of the thermocline. The warm water is in direct contact with the ice shelf, driving a mean melt rate of 4.4 m a^{-1}, which is equivalent to a freshwater volume of 6.2 km^3 a^{-1}. These values are an order of magnitude smaller than results for the default geometry (highlighted in Figure 6a), primarily because the mean ocean speed is low ($\bar{u}_O = 0.016$ m s^{-1}) due to the shallow slope of the ice base and the negligible buoyancy forcing. In addition, the different grounding line position reduces the area of the ice base available for melting by about 60%.

For $W > 0$ m, the grounding line is fixed at $y = 0$ km, where the ice becomes afloat at a depth of 1000 m. The evolution of the melt rate with W (gray curve in Figure 6a) is characterized by two distinct regimes: (i) For $0 < W \leq 150$ m, the total melt water volume increases linearly with W, and a maximum of about 108 km^3 a^{-1} is reached for $W = 200$ m; and (ii) for $W > 200$ m, the freshwater flux remains approximately constant, and mean melt rates are insensitive to changes in W. This threshold behavior suggests a rapid increase of melt rates at the onset of cavity formation, and the development of a relatively steady regime once the gap exceeds $W = 200$ m. During this evolution, the dominant changes in the melt rate occur for the region upstream of the ridge crest, as can be seen in Figure 7. This area also produces about 90% of the total meltwater volume (black line in Figure 6a).

The conductive heat flux into the ice shelf $\rho_I c_{pI} \kappa_I (T_b - T)/H_I$ in equation (2) is usually small compared with the latent heat $m\rho_O L$ [*Holland and Jenkins*, 1999; *Sergienko et al*., 2013] and can therefore be neglected. Melt rates are determined approximately by the simplified expression:

$$m = C\gamma_T (T - T_b), \tag{6}$$

where constant parameters have been combined into $C = \frac{c_{pO}}{L}$. The basal melt rate m is proportional to the product of two factors: the exchange velocity at the ice-ocean interface (γ_T), and the thermal driving (the difference between ambient ocean temperature and the local freezing temperature at the ice-ocean interface, $T - T_b$). According to equation (6), the increase and subsequent stabilization of m with increasing values of W, as depicted in Figure 6a, is the result of a change in γ_T, or $T - T_b$, or both.

Spatial averages of γ_T and $T - T_b$ are presented in Figure 6b; light colors represent averages over the entire ice shelf, dark colors cover the region with a relative change in melt larger than 1%. The increase of $\bar{\gamma}_T$ with W reflects a rise in the friction velocity at the ice-ocean interface, which coincides with a more vigorous barotropic circulation that spins up in the inner cavity. The depth-integrated barotropic stream function, which is shown by the contours in Figure 7, gradually strengthens, with maxima at 0.2 Sv for $W = 50$ m and 0.7 Sv for $W = 200$ m. The change in volume transport partly originates from a 25% increase in cavity cross section as the ice shelf thins, but the dominant cause is a doubling of the average zonal speed, from 3.7 mm s^{-1} for $W = 50$ m to 7.6 mm s^{-1} for $W = 200$ m. Since the flow is approximately geostrophic, the increase in zonal speed can be related to changes in the stratification. In particular, the meridional density gradients steepen, as the mixed layer thins and rises and the pycnocline is pushed upward by the dense bottom layer. This can

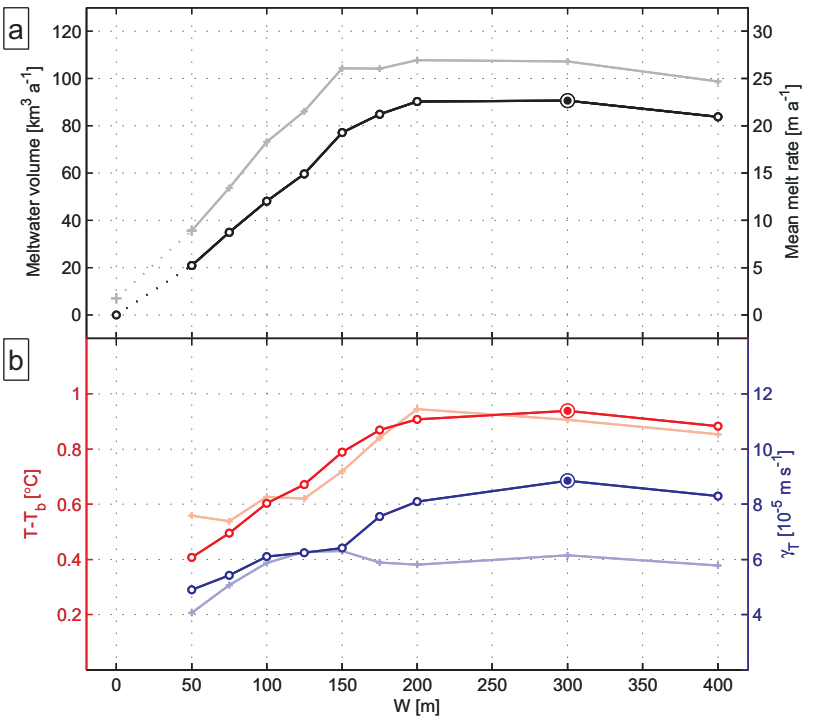

Figure 6. (a) Spatially integrated melt rates over the entire ice shelf (gray line) and the region where relative changes in melt between $W = 50$ m and $W = 400$ m exceed 1% (black line), as a function of W. The black dot highlights the meltwater volume for the default geometry, presented in section 3. (b) Red and blue lines show spatial averages of the exchange velocity at the ice-ocean interface (γ_T) and ocean thermal driving ($T - T_b$), as a function of W. Light red and blue correspond to averaged values for the entire ice shelf, dark red and blue correspond to averaged values for the region where relative changes in melt exceed 1%.

be seen in Figure 8, which illustrates the temperature and salinity along zonal section B at the ridge crest (left column) and along meridional section A in the middle of the domain (right column) for values of W ranging from 50 to 200 m.

In combination with the enhanced cyclonic circulation in the inner cavity, the meridional flow at the ridge evolves from weakly overturning into a barotropic current. For small gaps, the zero contour of the barotropic stream function follows the ridge crest (Figure 7), indicating a negligible net flow into the inner cavity. There is a northward current in the ice-ocean boundary layer, and an underlying southward current close to the seabed (not shown). For increasing values of W, the zero contour of the stream function diminishes, as the meridional flow at the ridge evolves into a more barotropic circulation. This circulation advects warm bottom water inshore in the east and center of the domain, and transports cold meltwater offshore along the western boundary (e.g., Figure 4a).

Concurrent with these changes in the cavity and boundary layer circulation, the thermal driving increases by about 130% (Figure 6b). For $W = 50$ m, the shallow water column at the ridge crest causes the ice shelf boundary layer to extend down to the ocean floor. This creates a barrier of cold (-1.3°C) and fresh (33.8) water which obstructs the flow of warm bottom water across the ridge (Figures 8a and 8b). Although for $W = 50$ m a small influx of warm water still persists at the eastern boundary, this water is cooled and freshened by mixing with the meltwater layer, resulting in strongly modified ocean conditions ($T = 0.3$°C, $S = 34.4$) in the inner cavity. The limited supply of heat to the ice base prevents strong melting and suppresses the buoyancy driven flow.

As the ice shelf thins and the gap between the ice base and the ridge increases, the bottom of the boundary layer rises, and mixing between colder meltwater and inflowing warm water diminishes (Figures 8c–8h). Average hydrographic properties in the inner cavity evolve from ($T = 0.3$°C, $S = 34.4$) for $W = 50$ m to ($T = 1.1$°C, $S = 34.65$) for $W = 200$ m. Once the water column thickness at the ridge crest exceeds the thickness of the mixed layer, bottom waters flowing into the inner cavity remain largely unmodified, and hydrographic properties in contact with the deepest part of the ice shelf become independent of W. The water

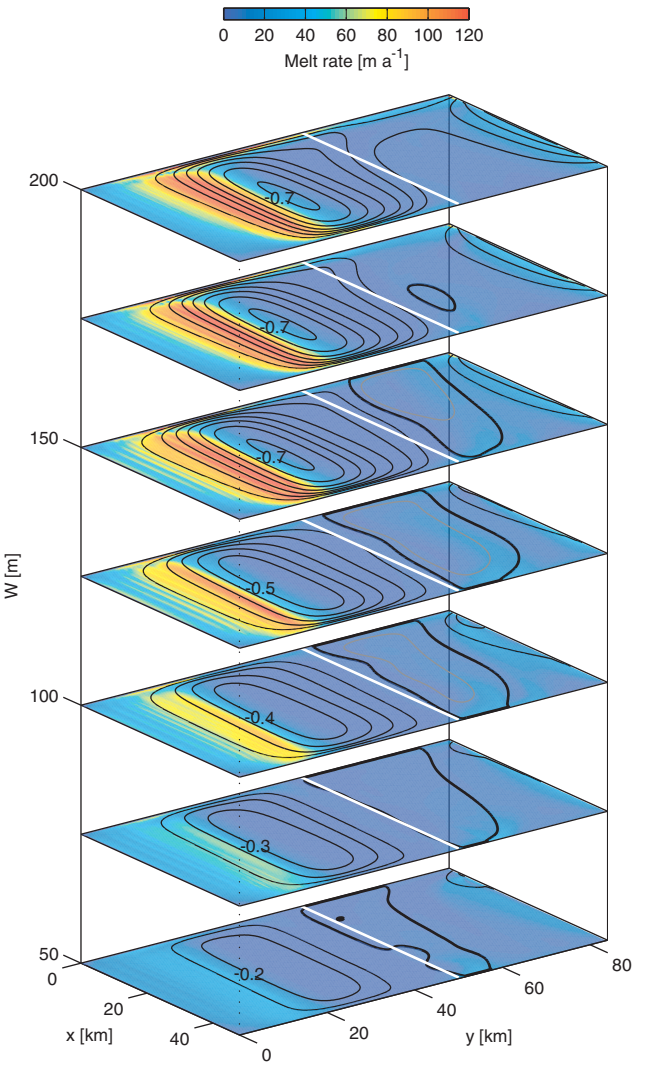

Figure 7. Melt patterns for ice shelf geometries with W ranging from (bottom) 50 m to (top) 200 m. Contours show the depth integrated barotropic stream function; thick black lines represent zero net meridional transport; thin solid lines correspond to a negative stream function and are spaced 0.1 Sv apart; thin gray lines correspond to the 0.1 Sv contour. White lines indicate the position of the ridge crest.

column in the inner cavity reaches a steady stratification, and the geostrophically balanced flow remains unaltered for $W > 200$ m. This results in constant values for both $T - T_b$ and γ_T, and therefore, constant melt rates (Figure 6a).

Further temporal changes to the stratification, circulation and melt rates can be controlled by other geometrical factors, such as variations in the depth and position of the grounding line or the slope of the ice base (not explicitly considered in this study), or by variations in the far-field hydrographic properties of the ocean, which will be investigated next.

5. Sensitivity of Melt Rates to Pycnocline Depth

Results from a survey underneath the ice shelf in 2009 [*Jenkins et al.*, 2010a] have shown that a layer of warm bottom water persists across the ridge top, separating the ice shelf boundary layer from the seabed and delivering weakly modified CDW to the inner cavity. Along its various tracks, Autosub has measured a gap between the ridge and the ice base that varies from around 300 m to <200 m in at least one point at the shallower northern part of the cavity. Additional constraints from gravimetric data provide a lower limit on the water column thickness at the ridge which is close to 200 m (see Figure 1). When compared to the $W = 200$ m threshold found in the previous section, this suggests that the PIG ice shelf has passed the transition from a geometrical dependence of melt rates to a regime where meltwater production is independent of W.

Although the onset of the current retreat and thinning of PIG remains the subject of investigation, an increased ocean heat content at the ice base related to the enhanced transport of CDW toward the PIG grounding line is thought to be the main driver [*Jenkins et al.*, 2010a; *Jacobs et al.*, 2011]. In order to assess the sensitivity of modeled melt rates to changes in the ocean heat content, and to quantify the relative importance compared with changes in the ice shelf geometry, we present the results from a sensitivity study in which the thermocline is lowered by 100 and 200 m, respectively (Figure 3). In order to preserve the separation between the top layer of cold and fresh winter water and the bottom layer of warm and saline CDW in keeping with observations (Figure 3), we synchronously move the halocline down by 100 and 200 m.

For each of the hydrographic forcings at the boundary, the total meltwater volume as a function of W is presented in Figure 9. For a fixed cavity geometry, i.e., a fixed value of W, the freshwater flux decreases in response to a lower pycnocline. The relative change between (T_{600}, S_{600}) and (T_{700}, S_{700}) is -15% or less,

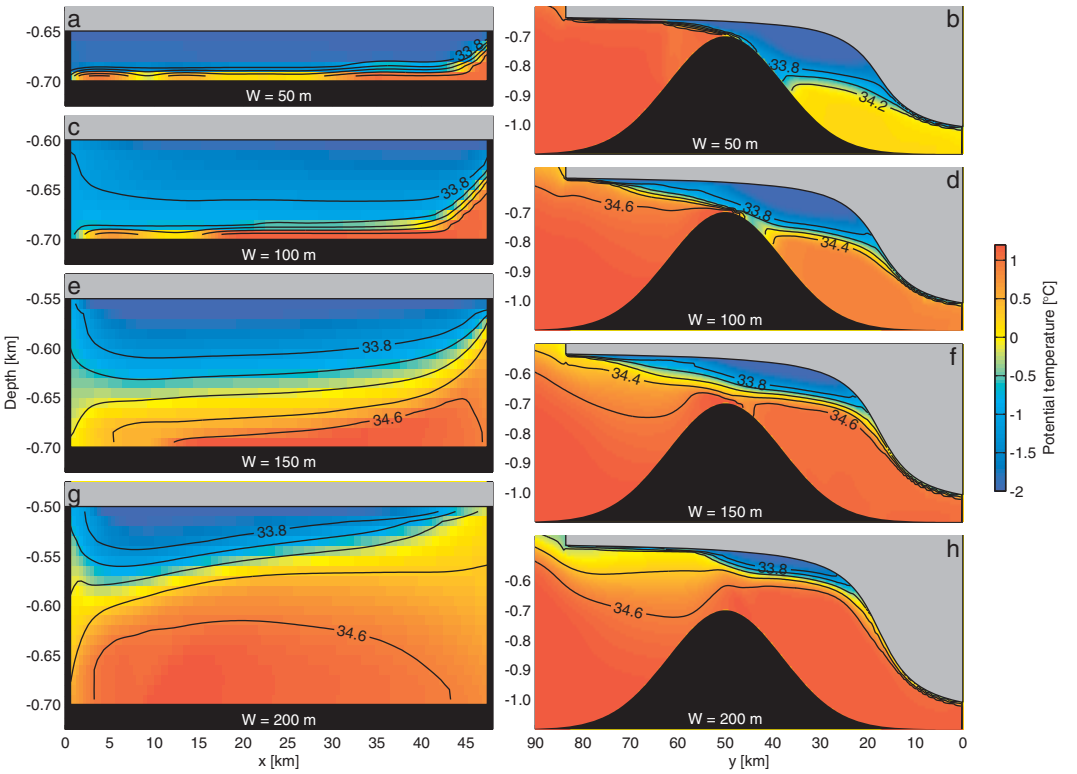

Figure 8. (left) West-east sections of temperature and salinity at the ridge crest (section A) for (a) $W = 50$ m to (g) $W = 200$ m. (right) The corresponding north-south sections along the middle of the domain (section B). All simulations are forced at the northern boundary by the (T_{600}, S_{600}) hydrographic conditions. Note that in Figures 8b–8h, only the deepest part of the water column is shown, as we are not interested in conditions next to the ice front. Also the part of the domain with $y \geq 90$ km is discarded.

and the relative change between (T_{600}, S_{600}) and (T_{800}, S_{800}) ranges from -30% to -40%. The decrease in melt rate in response to a lower thermocline can be directly attributed to an overall reduction in thermal forcing at the ice-ocean interface, as a smaller area of the ice shelf is exposed to warm bottom water, and less or no CDW is able to flow across the ridge to reach the ice base.

The melt rate exhibits a threshold behavior irrespective of the depth of the pycnocline, i.e., m increases linearly at the onset of cavity formation, and remains constant once the gap between the ice base and the bathymetry is sufficiently large. This confirms the purely geometrical nature of the transition, and emphasizes its robustness with respect to changes in the hydrographic forcing. For small values of W, there is little exchange between the far-field ocean and waters inshore of the ridge, and mixing with meltwater leads to cold and fresh conditions in the inner cavity (see Figures 10a–10d). As the ice shelf thins, exchange between waters offshore and inshore of the ridge is enhanced, and the dependency of the cavity hydrography and melt rates on the far-field forcing becomes stronger. Once the meltwater plume decouples from the ridge between $W = 100$ m and $W = 200$ m, mixing between the inflowing warmest waters and outflowing meltwater remains unchanged, and a constant stratification and circulation are established which results in constant melt rates in the inner cavity.

The steady stratification for $W \geq 200$ m differs significantly for different depths of the pycnocline, as shown in Figure 8h for (T_{600}, S_{600}) and in Figures 10g and 10h for (T_{700}, S_{700}) and (T_{800}, S_{800}). In the default case with (T_{600}, S_{600}), the top of the CDW layer lies 100 m above the ridge crest, and warm bottom water replenishes the inner cavity. The temperature and salinity averaged over the bottom 20 m of the water column inshore of the ridge are 1.12°C and 34.68, which is close to the values 1.2°C and 34.7 imposed at the northern boundary. For (T_{700}, S_{700}), the bottom of the pycnocline and the ridge crest are at equal depth, though zonal density gradients still drive a small southward flux of CDW across the ridge. This can be seen in Figure 10e, which shows an isolated current at the top of the ridge, and average temperature and salinity conditions at

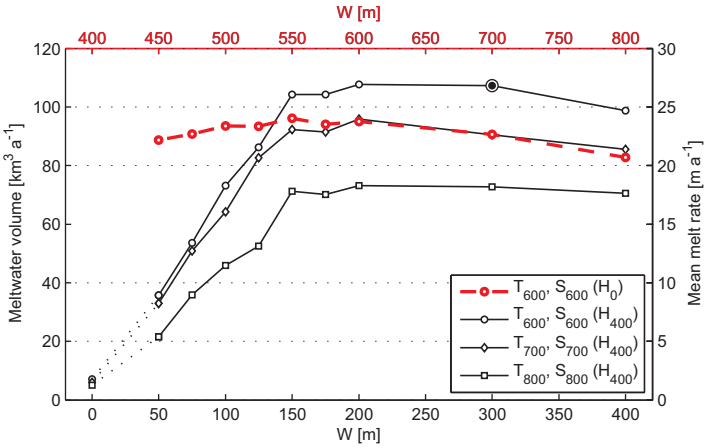

Figure 9. Black lines illustrate the dependence of the melt rates on *W* for different depths of the pycnocline bottom (600, 700, and 800 m, respectively). All results are for a 400 m high ridge. The dashed red line represents the evolution of the melt rates with *W* for a flat bathymetry and pycnocline bottom at 600 m.

the bottom of the inner cavity are 1.08°C and 34.67. For (T_{800}, S_{800}), the pycnocline bottom lies 100 m below the ridge, and only colder intermediate waters are in contact with the ice base. Average temperature and salinity in the bottom layer drop to 0.87°C and 34.6.

The strong variability in melt rates with pycnocline depth underlines the role of the subglacial ridge as a topographic barrier which modulates the inflow of CDW toward the grounding line. As the thermocline bottom at the PIG ice front naturally fluctuates around the depth of the ridge top, this ice shelf is particularly

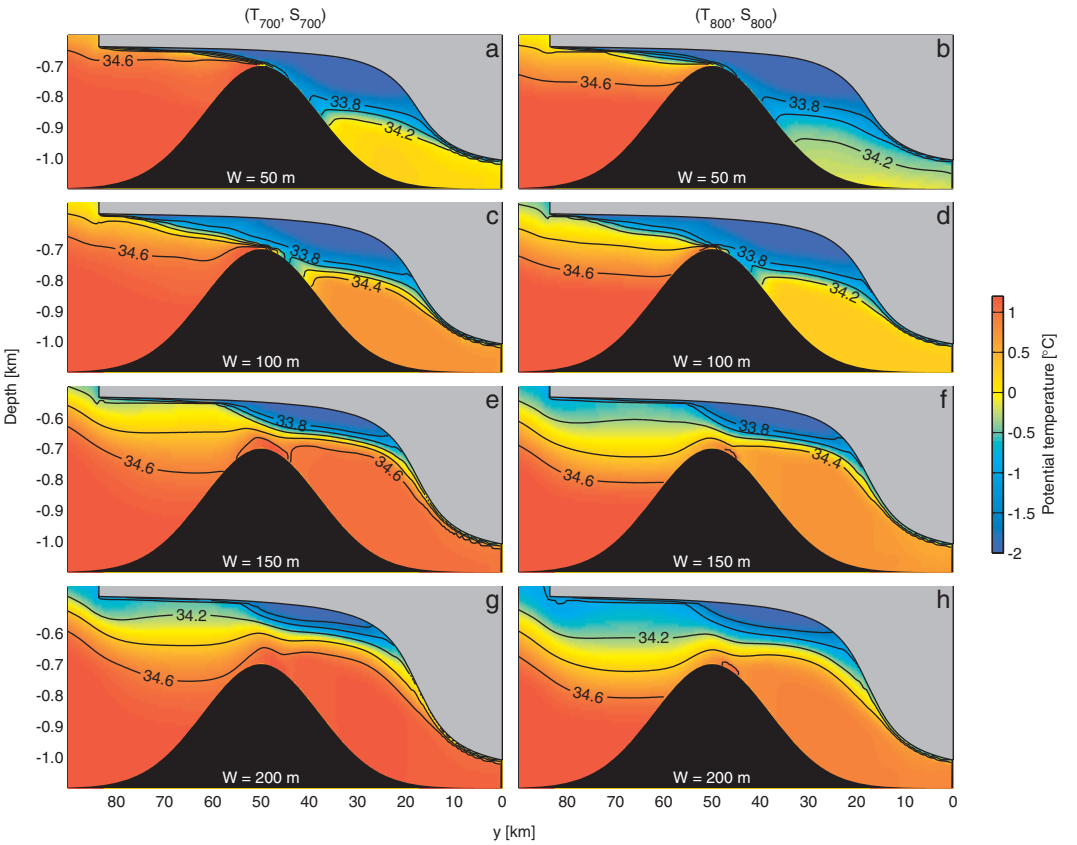

Figure 10. The left column shows the evolution of temperature and salinity with *W* along the middle of the domain (section B), with (T_{700}, S_{700}) forcing at the northern boundary. The right column is analogous but for the (T_{800}, S_{800}) forcing.

vulnerable to variability in CDW inflow and to large changes in the melt rate [*Dutrieux et al*., 2014]. In our simplified setup, meltwater production changes by about 30% in response to hydrographic conditions that simulate the shallow 2009 pycnocline and deep 2012 pycnocline. However, observations of meltwater transport in 2009 and 2012 at the PIG ice front indicate an even larger sensitivity of about 50%. One possible explanation for this discrepancy between idealized model results and observations is an incorrect representation of the height of the ridge. Although we have shown that the relative depth of the pycnocline bottom and the ridge top is an important factor in controlling the melt rate, the actual height of the ridge will also influence the sensitivity of melt rates to pycnocline depth. For example, in the extreme limit of a flat bathymetry, we expect less variability in the melt rates as warm bottom waters have direct access to the ice base irrespective of the pycnocline depth.

6. Sensitivity of Melt Rates to Height of the Ridge

In all simulations so far, the height of the subglacial ridge was kept constant at a value of $H = 400$ m. This choice was based on the comparison with a cross section of the bed along the flow direction of the ice shelf, obtained by a downward-looking echosounder on the Autosub3 submersible. At other places, the bathymetry underneath the PIG ice shelf has been estimated with the help of gravimetric measurements [*Muto et al*., 2013], and the depth of the ridge crest was found to vary between -800 and -600 m with an uncertainty of 100 m or more. Given the uncertainties about the bed topography, we investigate the sensitivity of our results to H.

A good starting point is the extreme limit in which $H = 0\ m$. In the absence of any subglacial terrain, deep waters extend uninterrupted from the northern boundary of the domain to the grounding line of the ice, where they set the ambient ocean conditions that drive the melt rate. There is no topographically trapped recirculation of ocean water in the inner cavity, and the flow follows a single cyclonic circulation pattern with inflow in the east and outflow in the west, similar to patterns observed in previous modeling studies [*Grosfeld et al*., 1997; *Losch*, 2008; *Holland et al*., 2008a; *Little et al*., 2009]. Similar to section 4, we compute the melt rates for a series of ice drafts with varying depth (parameterized by W), as depicted in Figure 2, but with a flat bathymetry instead. Results for these simulations are represented by the dashed red curve in Figure 9. For the considered range of W, the meltwater volume remains approximately constant, with an increase of about 8% between $W = 450$ m and $W = 550$ m, and a subsequent decrease of 15% between $W = 550$ m and $W = 800$ m. These small variations result from a balance between decreasing values of $T - T_b$ as the bottom of the ice shelf is raised into colder water, and increasing values of u_* as the slope of the ice draft between $x = 10$ km and $x = 30$ km steepens. The threshold behavior that was observed in the presence of a subglacial ridge is absent because the meltwater plume does not interact with the bathymetry, and melt rates are determined by the geometry of the ice draft only. For $W < 550$ m, melt rates are generally higher than in the presence of a subglacial ridge, as warm waters drive a stronger circulation in the inner cavity. For $W \geq 550$ m, the meltwater volume is about 10% lower than in the presence of a subglacial ridge due to smaller friction velocities at the ice-ocean interface, in particular in the inner cavity where the ridge gives rise to a vigorous cyclonic circulation.

In addition to changes in the ice draft, we can test the sensitivity of melt rates to changes in the pycnocline depth for a variety of seabed ridges. The results for H_0 are represented by the dashed red line in Figure 11. The response is linear to a good approximation, with a doubling of the melt rates between (T_{900}, S_{900}) and (T_{500}, S_{500}). Raising of the pycnocline gradually exposes a larger section of the ice base to warmer waters, and spatial changes to $T - T_b$ and u_* strongly reflect this warming. The area exposed to warm waters increases approximately linearly, hence explaining the linear trend in total meltwater volume.

A similar analysis can be done for different heights of the ridge. As described in section 2.2 and depicted in Figure 4b, we study two cases in which the ridge is raised (H_{500}) or lowered (H_{300}) by 100 m as compared to the default case (H_{400}), while keeping the gap between the ice and the bed constant at $W = 300$ m. For each value of H, the simulated meltwater volume as a function of the pycnocline depth is shown in Figure 11.

For a fixed pycnocline depth, melt rates generally decrease with increasing values of H, which is consistent with the fact that a higher ridge forms a stronger topographic barrier, hence reducing the flux of warm

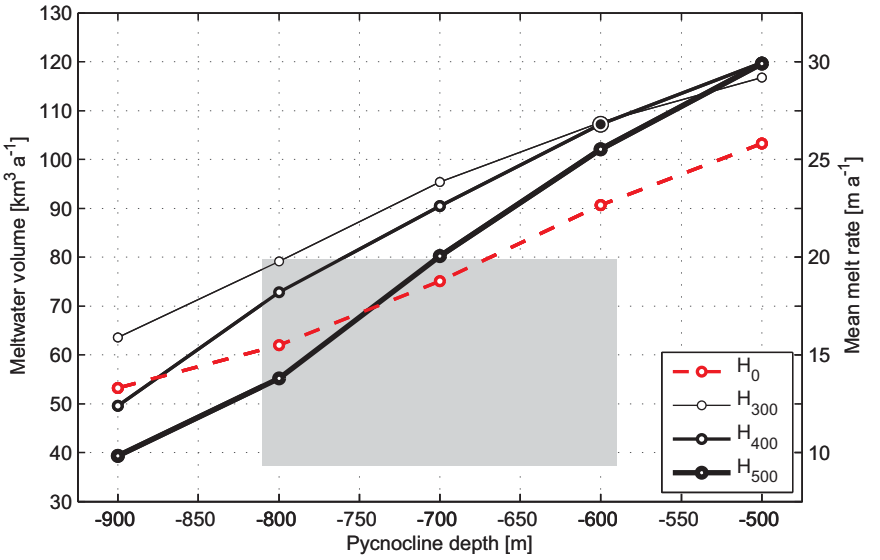

Figure 11. Solid lines show the sensitivity of the melt rate to pycnocline depth for different heights of the subglacial sill, i.e., H_{300}, H_{400}, and H_{500}. The dashed red line shows results for a flat bathymetry. The gray shaded area roughly delineates observational constraints on the pycnocline depth and meltwater output at the PIG ice front, based on a climatology of observations [*Dutrieux et al.*, 2014]. The lower limit corresponds to the 2012 deep pycnocline, the upper limit to the 2009 shallow pycnocline.

bottom water toward the ice base. As a result, a decrease in the thermal driving controls the drop in melt rates, whereas the exchange velocities remain relatively constant. With increasing values of H, the sensitivity of the meltwater production to changes in the pycnocline becomes stronger, with a 36% increase in meltwater production between (T_{800}, S_{800}) and (T_{600}, S_{600}) for H_{300}, a 47% increase for H_{400} and a 85% increase for H_{500}. The strongest variability in melt rates is thus found for the highest ridge, H_{500}, and the modeled sensitivity of 85% is comparable to the observed value of 110% for a deepening of the pycnocline between 2009 and 2012 [*Dutrieux et al.*, 2014].

7. Discussion

A key assumption in our model experiments is the choice of cavity geometries. They are not restricted by ice dynamics contraints, and therefore might not represent a fully realistic retreat scenario. In particular the fixed position of the grounding line at $y = 0$ km can be seen as a limitation to our experiments. However, the principle aim of this work is to investigate the impact of changes to the gap between the ice base and the ridge crest, which will widen irrespective of the retreat scenario. In order to address some of these constraints, we construct an alternative series of ice drafts corresponding to a uniform raising or lowering of the default W_{300} profile. This preserves the slope of the ice draft, and shifts the grounding line downstream (lowering) or upstream (raising). Calculations of the total meltwater production show a threshold behavior identical to Figure 6a, even though a small fraction of the change can be explained by the grounding line movement and a change in the ice shelf area available for melting (not shown).

Inherently, the ocean-ice shelf system is a coupled system, and mutual interactions between both components determine their changes. A static treatment of the ice shelf and the use of steady state ocean properties, adopted in this study, is therefore questionable. This is an issue that requires particular attention in a rapidly changing environment such as the PIG grounding zone, and requires the coupling between ice and ocean dynamics with a model that resolves the vertical ocean dimension. Potential questions that could be answered through a coupled approach are (1) how does the cavity geometry change throughout a melt-driven retreat from a subglacial sill, and (2) how do glaciological and oceanographic drivers compare during such a retreat. The latter question is particularly important in the light of recent studies that address the stability of grounding lines on reverse bed slopes, such as [*Favier et al.*, 2014] or [*Gudmundsson*, 2012]. A constant parameterization of melt rates is assumed in those studies, which is unlikely to hold in scenarios where the retreat from a subglacial ridge is considered.

In our idealized setup, transverse (x) variations in the geometry have been discarded. However, they likely, have a non-negligible effect on the ocean dynamics, as variations in the elevation of the ridge and water column thickness along the ridge crest influence the ice-ocean dynamics and sensitivity to changes in ocean forcing. More realistic models, such as the one presented by *Dutrieux et al*. [2014], also fail to simulate the high observed sensitivity, suggesting further deficiencies in the model geometry, forcing, and representation of ice-ocean interactions. The different behavior for H_{400} and H_0 in Figure 9, and the varied response to pycnocline depth with H in Figure 11 emphasise that accurate knowledge of the seabed is essential for models that aim to simulate the response of ice shelf melting to ocean variability.

The MITgcm has a number of numerical settings which have a potential impact on the simulated results. In particular, settings that affect the vertical mixing might influence the value of W for which the meltwater plume decouples from the ridge, hence shifting the threshold in Figure 6a to higher W (thicker meltwater layer) or lower W (thinner meltwater layer). The grid resolution was chosen to be eddy resolving in the horizontal (400 m), and sufficiently high in the vertical (10 m) to resolve a shallow 50 m water column at the ridge crest. Simulations with a 20 m vertical resolution did not lead to significantly different results. Vertical mixing was parameterized by the scheme of *Pacanowski and Philander* [1981], which defines the viscosity and diffusion parameters as a constant background level plus a Richardson number-dependent part. We tested changing these parameters by several orders of magnitude and found that the results were not qualitatively altered.

8. Conclusions

This study addresses the importance of the cavity geometry, determined by both the ice draft and the bathymetry, for the simulation of ice-ocean interactions beneath Pine Island Glacier. As it is challenging to obtain comprehensive geometrical data for the under-ice cavity, insights into the geometrical controls were obtained through idealized model simulations. In particular, we have quantified the importance of a seabed ridge that divides the cavity in two, and strongly regulates the melt rates. As local highs in the bed topography act as stable grounding line positions for the ice sheet, it is likely that such features are commonly present underneath other glaciers around the ice sheet margin. The observed thinning and retreat of many of these glacier systems could expose seabed features similar to that beneath Pine Island Glacier, and results from this study are therefore widely relevant.

Results show that the seabed ridge acts as a topographic barrier which prevents warm and saline deep water from reaching the ice base directly. However, the barrier only protects the ice shelf and prevents high melt rates when the bottom of the pycnocline sits well below the ridge crest. For a pycnocline at shallow or intermediate depths, warm deep water fills the inner cavity, and the topography induces a recirculation that tends to enhance friction at the ice-ocean interface, causing average melt rates that are 10% higher than in the absence of a ridge. Observations show that the depth of the pycnocline at the Pine Island Glacier ice front varies at interannual timescales, which leads to a strong variability in the melt rates. We find that this sensitivity crucially depends on the height of the sill, and accurate knowledge about the topography is therefore required in order to simulate the correct response of the melt rates to changes in the ocean forcing. In the absence of a ridge, the sensitivity to pycnocline depth is suppressed.

The thinning of Pine Island Glacier and the associated inland migration of its grounding line has led to fast temporal changes to the cavity geometry. In this work, we have identified a geometrical threshold behavior that suggests a strong linear increase in melt rates after the decoupling of the ice base from the ridge. This implies a runaway behavior once the retreat is initiated, as thinning leads to higher melt rates and further thinning. This feedback mechanism has the potential to shorten the glaciological timescales at which grounding lines are expected to migrate down a reverse bedslope, leading to a rapid initial retreat and destabilization of the ice shelf. However, further evidence for such a mechanism requires investigation using a 3-D coupled ice-ocean model. Once the ice shelf has sufficiently thinned, and the gap between the ice and the ridge top exceeds 200 m, melt rates enter a stable regime. Processes that determine the melt rate are then modulated by the oceanographic conditions in the vicinity of the ice shelf, and other geometrical changes to the cavity, such as the migration of the ice to deeper terrain. Pine Island Glacier currently sits in such a regime.

Acknowledgment
P.D. and J.D.R were supported by NERC grants NE/G001367/1 and NE/H02333X/1.

References

Assmann, K. M., A. Jenkins, D. R. Shoosmith, D. P. Walker, S. S. Jacobs, and K. W. Nicholls (2013), Variability of Circumpolar Deep Water transport onto the Amundsen Sea continental shelf through a shelf break trough, *J. Geophys. Res.*, *118*, 6603–6620, doi:10.1002/2013JC008871.

Cook, A., and D. G. Vaughan (2010), Overview of areal changes of the ice shelves on the Antarctic Peninsula over the past 50 years, *Cryosphere*, *4*(1), 77–98, doi:10.5194/tc-4-77-2010.

Dutrieux, P., D. G. Vaughan, H. F. J. Corr, A. Jenkins, P. R. Holland, I. Joughin, and A. Fleming (2013), Pine Island Glacier ice shelf melt distributed at kilometre scales, *Cryosphere*, *7*(2), 1591–1620, doi:10.5194/tcd-7-1591-2013.

Dutrieux, P., J. De Rydt, A. Jenkins, P. R. Holland, H. Kyung Ha, S. Hoon Lee, E. J. Steig, Q. Ding, E. P. Abrahamsen, and M. Schroeder (2014), Strong sensitivity of Pine Island Ice-Shelf melting to climatic variability, *Science*, *343*(6167), 174–178, doi:10.1126/science.1244341.

Gladish, C. V., D. M. Holland, P. R. Holland, and S. F. Price (2012), Ice-shelf basal channels in a coupled ice/ocean model, *J. Glaciol.*, *58*(212), 1527–1544, doi:10.3189/2012JoG12J003.

Grosfeld, K., R. Gerdes, and J. Determann (1997), Thermohaline circulation and interaction between ice shelf cavities and the adjacent open ocean, *J. Geophys. Res.*, *102*(C7), 15,595–15,610, doi:10.1029/97JC00891.

Heimbach, P., and M. Losch (2012), Adjoint sensitivities of sub-ice shelf melt rates to ocean circulation under Pine Island Ice Shelf, West Antarctica, *Ann. Glaciol.*, *53*(60), 59–69, doi:10.3189/2012/AoG60A025.

Holland, D. M., and A. Jenkins (1999), Modeling thermodynamic ice ocean interactions at the base of an ice shelf, *J. Phys. Oceanogr.*, *29*, 1787–1800.

Holland, D. M., R. H. Thomas, B. De Young, M. H. Ribergaard, and B. Lyberth (2008a), Acceleration of Jakobshavn Isbrae triggered by warm subsurface ocean waters, *Nat. Geosci.*, *1*(10), 659–664.

Holland, P. R., A. Jenkins, and D. M. Holland (2008b), The response of ice shelf basal melting to variations in ocean temperature, *J. Clim.*, *21*(11), 2558–2572, doi:10.1175/2007JCLI1909.1.

Jacobs, S. S., H. H. Hellmer, and A. Jenkins (1996), Antarctic ice sheet melting in the Southeast Pacific, *Geophys. Res. Lett.*, *23*(9), 957–960.

Jacobs, S. S., A. Jenkins, C. F. Giulivi, and P. Dutrieux (2011), Stronger ocean circulation and increased melting under Pine Island Glacier ice shelf, *Nat. Geosci.*, *4*(6), 1–5, doi:10.1038/ngeo1188.

Jenkins, A., H. H. Hellmer, and D. M. Holland (2001), The role of meltwater advection in the formulation of conservative boundary conditions at an ice-ocean interface, *J. Phys. Oceanogr.*, *31*(1), 285–296.

Jenkins, A., P. Dutrieux, S. S. Jacobs, S. D. McPhail, J. R. Perrett, A. T. Webb, and D. White (2010a), Observations beneath Pine Island Glacier in West Antarctica and implications for its retreat, *Nat. Geosci.*, *3*(7), 468–472.

Jenkins, A., K. W. Nicholls, and H. F. Corr (2010b), Observations and parameterization of ablation at the base of Ronne ice shelf, Antarctica, *J. Phys. Oceanogr.*, *40*, 2298–2312, doi:10.1175/2010JPO4317.1.

Joughin, I., B. E. Smith, and D. M. Holland (2010), Sensitivity of 21st century sea level to ocean-induced thinning of Pine Island Glacier, Antarctica, *Geophys. Res. Lett.*, *37*, L20502, doi:10.1029/2010GL044819.

Ligtenberg, S. R. M., M. M. Helsen, and M. R. van den Broeke (2011), An improved semi-empirical model for the densification of Antarctic firn, *Cryosphere*, *5*(4), 809–819.

Little, C. M., A. Gnanadesikan, and M. Oppenheimer (2009), How ice shelf morphology controls basal melting, *J. Geophys. Res.*, *114*, C12007, doi:10.1029/2008JC005197.

Losch, M. (2008), Modeling ice shelf cavities in a z-coordinate ocean general circulation model, *J. Geophys. Res.*, *113*, doi:10.1029/2007JC004368.

Mankoff, K. D., S. S. Jacobs, S. M. Tulaczyk, and S. E. Stammerjohn (2012), The role of Pine Island Glacier ice shelf basal channels in deep-water upwelling, polynyas and ocean circulation in Pine Island Bay, *Antarctica, Ann. Glaciol.*, *53*(60), 123–128, doi:10.3189/2012AoG60A062.

Marshall, J., C. Hill, L. Perelman, and A. Adcroft (1997), Hydorstatic, quasi-hydrostatic, and nonhydrostatic ocean modeling, *J. Geophys. Res.*, *102*, 5733–5752.

Medley, B., et al. (2013), Airborne-radar and ice-core observations of annual snow accumulation over Thwaites Glacier, West Antarctica confirm the spatiotemporal variability of global and regional atmospheric models, *Geophys. Res. Lett.*, *40*, 3649–3654, doi:10.1002/grl.50706.

Muto, A., S. Anandakrishnan, and R. B. Alley (2013), Subglacial bathymetry and sediment layer distribution beneath the Pine Island Glacier ice shelf, West Antarctica, modeled using aerogravity and autonomous underwater vehicle data, *Ann. Glaciol.*, *54*(64), 27–32, doi:10.3189/2013AoG64A110.

Pacanowski, R. C., and S. G. H. Philander (1981), Parameterization of vertical mixing in numerical models of tropical oceans, *J. Phys. Oceanogr.*, *11*, 1443–1451.

Park, J. W., N. Gourmelen, A. Shepherd, S. W. Kim, D. G. Vaughan, and D. J. Wingham (2013), Sustained retreat of the Pine Island Glacier, *Geophys. Res. Lett.*, *40*, 2137–2142, doi:10.1002/grl.50379.

Payne, A. J., P. R. Holland, A. P. Shepherd, I. C. Rutt, A. Jenkins, and I. Joughin (2007), Numerical modeling of ocean-ice interactions under Pine Island Bay's ice shelf, *J. Geophys. Res.*, *112*, C10019, doi:10.1029/2006JC003733.

Pritchard, H. D., S. R. M. Ligtenberg, H. A. Fricker, D. G. Vaughan, M. R. van den Broeke, and L. Padman (2012), Antarctic ice-sheet loss driven by basal melting of ice shelves, *Nature*, *484*(7395), 502–505.

Rignot, E. J. (1998), Fast recession of a West Antarctic glacier, *Science*, *281*(5376), 549–551, doi:10.1126/science.281.5376.549.

Rignot, E., and K. Steffen (2008), Channelized bottom melting and stability of floating ice shelves, *Geophys. Res. Lett.*, *35*, L02503, doi:10.1029/2007GL031765.

Rignot, E., S. Jacobs, J. Mouginot, and B. Scheuchl, (2013), Ice-shelf melting around Antarctica, *Science*, *341*(6143), 266–270, doi:10.1126/science.1235798.

Scambos, T., T. Haran, M. Fahnestock, T. Painter, and J. Bohlander (2006), MODIS-based Mosaic of Antarctica (MOA) data sets: Continent-wide surface morphology and snow grain size, *Remote Sens. Environ.*, *111*(2), 242–257, doi:10.1016/j.rse.2006.12.020.

Schodlok, M. P., D. Menemenlis, E. Rignot, and M. Studinger (2012), Sensitivity of the ice-shelf/ocean system to the sub-ice-shelf cavity shape measured by NASA IceBridge in Pine Island Glacier, West Antarctica, *Ann. Glaciol.*, *53*(60), 156–162, doi:10.3189/2012AoG60A073.

Sergienko, O. V., D. N. Goldberg, and C. M. Little (2013), Alternative ice shelf equilibria determined by ocean environment, *J. Geophys. Res.*, *118*, 970–981, doi:10.1002/jgrf.20054.

Shepherd, A., D. Wingham, and E. Rignot (2004), Warm ocean is eroding West Antarctic Ice Sheet, *Geophys. Res. Lett.*, *31*, L23402, doi:10.1029/2004GL021284.

Shepherd, A., D. Wingham, D. Wallis, K. Giles, S. Laxon, and A. V. Sundal (2010), Recent loss of floating ice and the consequent sea level contribution, *Geophys. Res. Lett.*, *37*, L13503, doi:10.1029/2010GL042496.

Shepherd, A., et al. (2012), A reconciled estimate of ice-sheet mass balance, *Science*, *338*(6111), 1183–1189, doi:10.1126/science.1228102.

Thoma, M., A. Jenkins, D. Holland, and S. Jacobs (2008), Modelling Circumpolar Deep Water intrusions on the Amundsen Sea continental shelf, Antarctica, *Geophys. Res. Lett.*, *35*, L18602, doi:10.1029/2008GL034939.

Van der Veen, C. J. (1985), Numerical modelling of ice shelves and ice tongues, *Ann. Geophys.*, *4*(B), 45–54.

Vaughan, D. G., H. F. J. Corr, R. A. Bindschadler, P. Dutrieux, G. H. Gudmundsson, A. Jenkins, T. Newman, P. L. Vornberger, and D. Wingham (2012), Subglacial melt channels and fracture in the floating part of Pine Island Glacier, Antarctica, *J. Geophys. Res.*, *117*, F03012, doi:10.1029/2012JF002360.

Wahlin, A. K., X. Yuan, G. Bjork, and C. Nohr (2010), Inflow of warm circumpolar deep water in the central Amundsen shelf, *J. Phys. Oceanogr.*, *40*(6), 1427–1434, doi:10.1175/2010JPO4431.1.

Walker, D. P., M. A. Brandon, A. Jenkins, J. T. Allen, J. A. Dowdeswell, and J. Evans (2007), Oceanic heat transport onto the Amundsen Sea shelf through a submarine glacial trough, *Geophys. Res. Lett.*, *34*, L02602, doi:10.1029/2006GL028154.

Walker, D. P., A. Jenkins, K. M. Assmann, D. R. Shoosmith, and M. A. Brandon (2013), Oceanographic observations at the shelf break of the Amundsen Sea, Antarctica, *J. Geophys. Res.*, *118*, 2906–2918, doi:10.1002/jgrc.20212.